Chen, Y., Xu, Y., Xu, T., Si, S., Liang, X., Tian, X., Deng, Y., Chen, L., Wang, P., Xu, Y., Lan, H., Xiao, F., Li, W., Zhang, X., Yuan, X., Badal, J., Teng, J. (2015): Magmatic underplating and crustal growth in the Emeishan Large Igneous Province, SW China, revealed by a passive seismic experiment. - *Earth and Planetary Science Letters*, *432*, pp. 103–114.

DOI: http://doi.org/10.1016/j.epsl.2015.09.048

Magmatic underplating and crustal growth in the Emeishan Large Igneous Province, SW China, revealed by a passive seismic experiment

Yun Chen[a,*], Yigang Xu[b], Tao Xu[a], Shaokun Si[c], Xiaofeng Liang[a], Xiaobo Tian[a], Yangfan Deng[b], Lin Chen[a], Peng Wang[d], Yihe Xu[a,e], Haiqiang Lan[a], Fuhui Xiao[a], Wei Li[a,e], Xi Zhang[a], Xiaohui Yuan[f], José Badal[g], Jiwen Teng[a]

[a] State Key Laboratory of Lithospheric Evolution, Institute of Geology and Geophysics, Chinese Academy of Sciences, Beijing 100029, China

[b] State Key Laboratory of Isotope Geochemistry, Guangzhou Institute of Geochemistry, Chinese Academy of Sciences, Guangzhou 510640, China

[c] Department of Deep-sea Investigation, National Deep Sea Center, Qingdao 266061, China

[d] Institute of Earthquake Science, China Earthquake Administration, Beijing 100036, China

[e] University of Chinese Academy of Sciences, Beijing 100049, China

[f] Deutsches GeoForschungsZentrum GFZ, Telegrafenberg, 14473 Potsdam, Germany

[g] Physics of the Earth, Sciences B, University of Zaragoza, Pedro Cerbuna 12, 50009 Zaragoza, Spain

* Corresponding author. Tel.: +86 10 8299 8339; fax: +86 10 8299 8001.

E-mail address: yunchen@mail.iggcas.ac.cn (Y. Chen)

ABSTRACT

In an attempt to characterize the subsurface structure that is related to fossil mantle plume activity, a comprehensive geophysical investigation was conducted in the Emeishan Large Igneous Province (ELIP). The nature and geometry of the crust were examined within the scheme of the domal structure of ELIP, which comprises the Inner, Intermediate and Outer zones, which are defined on the basis of the biostratigraphy of pre-volcanic sediments. The bulk crustal properties within the Inner Zone are characterized by high density, high P-wave velocity, high Vp/Vs ratios and large crustal thickness. A visible continuous seismic converter is present in the upper part of the crust in the whole Intermediate Zone and the eastern part of the Inner Zone, but it is absent in the Inner Zone, where another seismic converter is observed in the lower part of the crust. The geometric configuration of these converters is attributable to the addition of mantle-derived melts to the pre-existing crust and subsequent interaction between them. The crustal geometry, which is delineated by the migrated image of receiver functions from the passive seismic experiment, and the crustal properties collectively suggest that a mafic layer of 15-20 km thickness and 150-180 km width exists at the base of the crust in the Inner Zone. Such a mafic layer reflects a vertical crustal growth through magmatic underplating at the base of the crust and intraplating within the upper crust. The salient spatial correlation between the deep crustal structure and the dome strongly supports a genetic link between crustal thickening and plume activity, if the pre-volcanic domal uplift is generated by the Permian Emeishan mantle plume. This arrangement is further supported by the consistency of the extent of crustal uplift estimated by isostatic equilibrium modeling and sedimentary data. This study therefore characterizes and provides evidence for a plume-modified crust in a large igneous province.

Keywords: receiver function; crustal property; magmatic underplating; crustal growth; mantle plume; Emeishan Large Igneous Province

1. Introduction

The Permian, which is characterized by emplacements of a number of large igneous provinces (LIPs), is an important period in the earth's history (Wignall et al., 2009). Recently, recognition of the potential role of LIPs in affecting biotic evolutionary pathways and metallogenic systems has led to growing interest in these provinces (Xu et al., 2014). The Emeishan flood basalt in SW China (Fig. 1) has been recognized as one of the major mafic LIPs (Xu et al., 2004; Xu et al., 2007). It was emplaced over a short time with a termination age of 259.1±0.5 Ma, which is very close to the Guadalupian-Lopingian Boundary (Zhong et al., 2014). Thus, it is possibly synchronous with a number of major global events during the late Paleozoic, such as the double mass extinctions, ocean superanoxia, sharp C and Sr isotopic excursions, sea-level drop and the Illawara geomagnetic reversal (Wignall et al., 2009; Xu et al., 2014). There are many mafic-ultramafic intrusions within the Emeishan LIP (hereafter ELIP) that host Fe-Ti-V and Ni-Cu-PGE deposits (Zhou et al., 2008), which have already become important targets for mineral exploration.

Over the past decade, multidisciplinary investigations have been conducted in ELIP on the origin of this LIP, the mineralization system associated with a mantle plume, and paleoclimatic reconstructions and their implications for the Permian mass extinctions. A mantle plume model has been used to explain the physical and chemical features of ELIP, including the eruption of high magnesian lavas and evidence for pre-volcanic crustal domal uplift. Xu et al. (2007) summarized the identifications of mantle plume in ELIP and argued that there would be at least seven pieces of evidence that support a Permian mantle plume origin for this province. Most of the evidence for the mantle plume is from geochemical, paleontological, paleomagnetic, and geochronological studies, but the geophysical constraints are very limited. Most of the seismic evidence for mantle plumes is confined to the modern, active hotspots such as Hawaii, Kerguelen, Iceland and Yellowstone (Montelli et al., 2004). The thermal effects of high temperature and low viscosity magma-derived and subsequent geophysical responses (especially low seismic velocity) within the deep interiors are the most important clues to tracing a modern mantle plume for seismic investigation. The ELIP is related to an ancient plume, whereas the thermal effects that are plume-derived would have decayed with a time constant of approximately 60 Myr (McKenzie, 1984). Since the termination of the volcanism, ELIP has traveled more than three thousand kilometers away from its putative source (Fig. 1), and the mantle has continuously cooled down for over 250 Myr. Both the thermal decay and the drifting away from the original site would result in great difficulty in tracing an ancient plume for geophysical investigation. Fortunately, as an archive of the earth's history, the solidified continental crust has the most possible ability to preserve the imprints of the earth's evolution, by its composition and structure (Hawkesworth et al., 2013). Thus, in this sense, the constraints on the crustal composition and geometric structure from the geophysical investigations could provide an opportunity to identify an ancient mantle plume. However, to understand the origin of an ancient LIP, great care must be taken when a real-time geophysical observation on the deep-seated and hence volatile structures (e.g., the mantle transition zone) is used as a discriminator (He et al., 2014).

In an attempt to trace the geological records that were left by the proposed ancient mantle plume, a series of geophysical investigations were conducted in ELIP discontinuously from November 2010 to April 2013. Four east-west trending profiles that are approximately along the latitude 27°N are involved in a COMprehensive investigation on ELIP: 1) a linear PASSive seismic array (COMPASS-ELIP experiment, ca. 850 km long); 2) a WIDE-angle reflection/refraction seismic profile (COMWIDE-ELIP experiment, ca. 650 km long); synchronous measurements of 3) GRAvity (COMGRA-ELIP experiment, ca. 800 km long) and 4) geoMAGnetism (COMMAG-ELIP experiment). In this paper, we will present observations of the crustal nature and geometry mainly from the COMPASS-ELIP experiment and discuss their implications in the origin of voluminous mafic basalts and the crustal growth mechanism in this igneous province.

2. Geological settings

The Permian Emeishan basalts are erosional remnants of voluminous mafic volcanic successions that are located at the western margin of the Mesoproterozoic Yangtze Craton and the southeastern margin of Tibet, SW China (Xu et al., 2004; Ali et al., 2005). They are exposed in a roughly rhombic area of 250,000 km^2 that is bounded by the Lijiang-Xiaojinhe thrust fault (LXF, F4 in Fig. 2) in the northwest and the Ailaoshan-Red River slip fault (ARF, F3 in Fig. 2) in the southwest. The thickness of the entire volcanic sequence in this province varies considerably, from over 5000 m in the west to a few hundred meters in the east (He et al., 2003). The province consists of dominant basaltic lavas and subordinate pyroclastic rocks. The Emeishan volcanic successions unconformably overlie the late middle Permian Maokou Limestone and are in turn covered by the uppermost Permian sediments in the east and west and by the upper Triassic or Jurassic sediments in the central part (He et al., 2003). Here, the carbonate beds of the underlying Maokou Formation have been systematically thinned by erosion toward the center of the flood basalt province, which suggests a pre-volcanic crustal domal uplift. The extent of erosion of the Maokou Formation indicates that ELIP can be divided into three roughly concentric zones (Fig. 2): the Inner, Intermediate, and Outer zones (He et al., 2003; He et al., 2010). The Inner Zone (INZ) has a radius of ca. 200 km, where the erosion of the Maokou Formation is most intensive and the uplift is estimated to be at least 500 m and probably could exceed 1000 m, and is considered to be the impact site of the rising plume head. The Intermediate Zone (IMZ) has a radius of 425 km, an average uplift of ca. 300 m and a modest extent of erosion. The Outer Zone (OTZ) has a radius of 800 km, a minimum uplift and a minor extent of erosion. Such a division of the domal structure is important because it provides a natural basis to subdivide ELIP (Xu et al., 2004; Campbell, 2005).

In addition, to the west of INZ, the tectonic feature is characterized by two roughly north-south trending right-lateral strike-slip faults: the Nujiang River fault (F1 in Fig. 2) and the Langcangjiang River fault (F2 in Fig. 2). This zone is the northernmost of the Southeast Asia extrusion system. Its active movement is mainly responsible for the eastward extrusion, which has been related to the India-Eurasia collision since the Cenozoic (Yin, 2010). Three large rivers (Nujiang, Langcang, and Jingsha rivers) course down from Southeast Tibet and travel in parallel through this area. Herein, this area is briefly called the Three-river Zone (TRZ) for simplification (Fig. 2).

3. Data and methods

The COMPASS-ELIP experiment was conducted along the latitude of 27^{o}N between Fugong in western Yunnan and Guiding in central Guizhou, crossing TRZ, INZ, IMZ, and OTZ from west to east (Fig. 2). The profile has a total length of ca. 850 km, and 59 seismographs (Reftek-130 data loggers plus Guralp CMG3-ESP sensors of 50Hz-30s/60s) were deployed with a station interval of ca. 15 km. According to the observation periods, the profile was divided into two segments: the West- and East-Lines. A total of 29 seismographs (namely, E01-E31, with the absence of E03 and E04 due to the inaccessibility of the Nushan Mountain in western Yunnan) were deployed for the West-Line between November 2010 and November 2011. After the completion of the experiment along the West-Line, 30 seismographs (namely, E32-E61) were then deployed along the East-Line from December 2011 to April 2013. During the two-phase observations, 579 and 398 earthquakes with a magnitude of greater than *Ms* 5.0 in the distance range of 30 to 90 degrees (Fig. 3) were recorded by the West-Line and East-Line arrays, respectively.

Teleseismic P-wave Receiver Functions (RFs) were calculated using time-domain iterative deconvolution of vertical and radial seismograms (Ligorria and Ammon, 1999). We obtained 6793 RFs (4503 for West-Line and 2290 for East-Line) for the 59 stations along the profile after eliminating those records for which the Moho Ps conversions have a low signal-to-noise ratio. The larger number of useful events and RFs for the West-Line mainly results from the higher earthquake activity in 2011. The stacked RFs (the summed trace of the move-out corrected RFs) for all 59 stations along the profile are shown in Fig. 4. The P and Moho converted Ps-phases can be observed very clearly. The delay time between the P and Ps converted phases fluctuates along the profile: approximately 6.0 s under TRZ, 7.0 s under INZ, 5.5 s under IMZ, and 4.5 s under OTZ (Fig.4). These delay time variations reflect the Moho topography and can be taken as the first-order constraints on the crustal thickness. The longer the delay time is, the greater the crustal thickness. In this sense, the large delay time suggests a thick crust in INZ.

4. Crustal structure of ELIP

With the advantage of suppressing the trade-off between the crustal thickness (H) and the bulk Vp/Vs ratio (κ), the H-κ stacking procedure (Zhu and Kanamori, 2000) has been used routinely for teleseismic RFs at each individual seismic station. At each station of the COMPASS-ELIP array, we first processed the available data set of RFs using the H-κ stacking method based on the averaged crustal P-wave velocity model (Fig. 5b) derived from the COMWIDE-ELIP experiment (Xu et al., 2015) (Fig. 5d), and estimated the standard errors of H and Vp/Vs ratio by the bootstrap method (Efron and Tibshirani, 1986) for 100 trials. To smooth out the rapid lateral variations within each zone, an arithmetic average and the standard errors of H and the Vp/Vs ratio were further calculated using a three-station sliding-average scheme. The lateral variations of H and the Vp/Vs ratio and their uncertainties along the profile are listed in Table 1 and are shown in Fig. 5e, f. In general, the uncertainties for H-κ stacking of stations in TRZ and INZ are much smaller than those in IMZ and OTZ because of a larger number of events and useable RFs in the West-line (Table 1). The average standard error of H and the Vp/Vs ratios from H-κ stacking for stations in TRZ and INZ is less than 1.1 km and 0.017, respectively.

To construct a depth-domain crustal conversion image, a migration scheme of Common Conversion Points (CCP) stacking (Yuan et al., 1997) was used to focus the converted signal from the time series of each RF to its relevant conversion point. In the traditional approach, the CCP-stacking migration needs a reference velocity model, and the IASP91 model (Kennett and Engdahl, 1991) is used widely. However, in this study, we used a modified model that was based on the crustal P-wave velocity (Fig.

5b) derived from the COMWIDE-ELIP experiment (Xu et al., 2015) and the crustal Vp/Vs ratio (Fig. 5f) from H-κ stacking. By comparing it with the IASP91 model (Fig. 6a), we found that the modified model (Fig. 6b) made the amplitudes focus better at the Moho discontinuity and manifest some intracrustal interfaces at certain depths. Therefore, the migrated image based on the modified velocity model provides a fine skeleton drawing of the geometric crustal structure. The signature of the Moho discontinuity in the migrated image (Fig. 5c) is well consistent with the depth that is estimated by H-κ stacking (Fig. 5e). Additionally, three other dominant signatures can be recognized within the crust (they will be interpreted as the underplating interface (UI), Conrad discontinuity (CD) and crystalline basement (CB) in the following section): 1) the signature at a depth of ca. 35 km in INZ (UI, in Fig. 5c), bounded by LXF (F4 in Fig. 2) and LYF (F5 in Fig. 2); 2) the signature at a depth of 20~25 km (CD, in Fig. 5c) in the east part of INZ and almost the whole IMZ, bounded by LYF and SZF (F8 in Fig. 2); 3) the signature at a depth of 15 km (CB, in Fig. 5c) bounded by SZF in the west, which corresponds to the noticeable tectonic feature of Shuicheng-Ziyun Aulacogen (SZA) in the western margin of OTZ. Both the Moho and these intracrustal signatures can also be recognized in the stacked RFs in time domain (Fig. 4).

5. Discussion

5.1. Spatial variations in the crustal thickness and Vp/Vs ratios

According to the results yielded by H-κ stacking at each station and the subsequent sliding-average along the profile (Fig. 5e, f), the following features of the variations in H and the Vp/Vs ratio are noted: 1) Both TRZ and INZ have a thick crust (50-60 km) and high Vp/Vs ratios (1.75-1.85); 2) IMZ has a lower crustal thickness (40-50 km) and moderate Vp/Vs ratios (1.70-1.80); 3) OTZ has a relatively thin crust (ca. 40 km) and low Vp/Vs ratios (1.65-1.75); and 4) Within the east part of INZ, the crustal thickness reaches a maximum of 60 km. In general, both the crustal thickness and the Vp/Vs ratios decrease progressively from west to east along the profile, which is roughly consistent with previous independent estimates from tomography (Xu and Song, 2010) and joint inversions of receiver functions and surface waves (Sun et al., 2014; Bao et al., 2015). For example, high Vp/Vs ratios and thick crustal thicknesses were also detected to the West of XJF by a seismic array south to our profile (Sun et al. 2014).

We plotted the values of H vs. Vp/Vs for each zone, to visualize their spatial variations (Fig. 7). Intriguingly, the data from different zones delineates distinct patterns, which are enclosed by the best-fitting ellipses with a criterion of minimum area. The center of the ellipse corresponds to the average H and Vp/Vs ratio of the zone. Noticeably, a relatively high average Vp/Vs ratio (ca. 1.77) and the largest crustal thickness (ca. 54 km) are located in INZ.

The Vp/Vs ratio is related to the mineralogy and composition and even to the physical state of the crust (Zandt and Ammon, 1995; Christensen, 1996). In general, either mafic/ultramafic compositions, fluids, high temperature, or partial melting will induce high Vp/Vs ratios. The surface heat flow, along with information about the thermal conductivity and heat production rate in the crust, is the essential data for understanding the crustal temperature (Tao and Shen, 2008). The heat flow distribution in the Chinese continent and its adjacent areas was mapped by Hu et al. (2000) and later updated by Tao and Shen (2008). Although the heat flow observations in China are still sparse and unevenly distributed, more than 35 available measurements in West and Central Yunnan (Tao and Shen, 2008) provided good constraints along our profile, especially for TRZ and INZ. We extracted the data along the latitude of 27°N from the heat flow dataset produced by Tao and Shen (2008). The lateral variation of the heat flow clearly shows a concave-shaped decrease at the center of the INZ relative to the adjacent regions, which basically forms a mirror-symmetric relationship with the variation in the Vp/Vs ratios (Fig. 5f). The feature of low heat flow and high Vp/Vs ratios, combined with the properties that are characterized by high gravity anomaly (Fig. 5a) high P-wave velocity (Fig. 5b) with no significant low velocity zone (LVZ) within the crust (Fig. 5d) in INZ, enables us to exclude the existence of massive fluids, permanent high temperatures and/or partial melting in the current crustal interior of INZ.

Alternatively, we propose that the high Vp/Vs ratios in INZ are most likely caused by the frozen mafic/ultramafic magmatic underplating that is associated with the ancient mantle plume. In general, the heat production in mafic/ultramafic rocks is at least one order of magnitude lower than that in felsic rocks (Furlong and Chapman, 2013). The replacement of felsic rocks with mafic or ultramafic rocks through magmatic underplating or igneous intrusion will reduce the heat production in the crust and thus will decrease the surface heat flow in the long term. This arrangement is again consistent with the low surface heat flow at the center area of the INZ (Fig. 5f). In contrast, given the high bulk crustal Vp/Vs ratio and high heat flow (Fig. 5f) in TRZ, we favor an interpretation of an *ongoing* addition of high-Vp/Vs materials into the crust, either a basaltic underplating related to upwelling that results from the eastward subduction of the Indian Plate beneath Burma Arc (Lei et al., 2009) or by a lower crustal flow that is related to the south-eastward escaping of the Tibetan deep crust (Royden et al., 1997).

5.2. Interpretations of the seismic signatures within the crust

Besides the Moho discontinuity, three other intracrustal signatures were recognized and described in section 4. With the caution that the interference of multiple conversions within crust could be present in the stacked RFs in time-domain (Fig. 4), and, hence in the migrated image in depth-domain (Figs. 5c, 6), these signatures are interpreted as seismic expressions of the crustal geometry of ELIP, which is depicted in Fig. 8.

5.2.1. Moho discontinuity

In most of the crustal studies, the RFs method images the Moho discontinuity with a high reliability. In our study, the signature of Moho discontinuity can be visibly recognized not only in the stacked RFs in time-domain (Fig. 4) but also in the migrated image in depth-domain (Figs. 5c, 6), which is characterized by strong continuous positive amplitudes at the corresponding time or depths. More specifically, two strong converters in OTZ are imaged both in both time- and depth-domains (Figs. 4 and 6). We interpret the shallower converter (ca. 4.5 s or ca. 40 km) as the Moho, and the deeper converter (close to 7.0 s or ca. 60 km) as an interface in the uppermost mantle in OTZ. We will discuss the details of the deeper converter and its implication in another paper. Assuming a perfect Airy-type crustal isostacy, the crustal thickness H can be estimated by

$$H = \frac{\rho_c}{\rho_m - \rho_c} h + H_0 \qquad (1)$$

where, ρ_c and ρ_m are the crustal and upper mantle densities (ca. 2.75 g/cm^3 and 3.20 g/cm^3 generally), respectively; h is the present-day topography; and H_0 is the reference crustal thickness (a global average of 33 km). In our case, the average topography (green line in the upper panel of Fig. 5c), which is computed by a running average along our profile within a radius of 60 km, is substituted, and then, the Airy Moho is obtained (green line in Fig. 5e). Except for INZ, to the first order, the Airy Moho matches the trends of the Moho that is estimated independently by H-κ stacking (Fig. 5e) or recognized from the RFs sections in time- and depth-domains (Figs. 4, 5c and 6). This match strongly suggests that the shallower converter in time- or depth-domains in OTZ should be the present-day Moho, which is also confirmed by the COMWIDE-ELIP experiment (Xu et al., 2015) (Fig. 5d) and another previous controlled-source seismic survey that was conducted in 1984 (Xiong et al., 1986). Meanwhile, the mismatch, where the Moho depth in INZ is much deeper than Airy Moho (Fig. 5e), strongly suggests the existence of a high-density crust in this zone. Generally, this feature of the Moho topography not only reflects the modern day processes related to the lateral variations of the surface elevations along the profile, but also reveals the distinct crustal property (high density) of INZ that is highly consistent with the feature of the gravity data (Fig. 5a).

5.2.2. *Crystalline basement (CB)*

The signature CB marks the strong positive amplitudes that appear at ca. 1.5 s (Fig. 4) or at the depth of ca. 15 km (Fig. 5c), with a horizontal extent of ca. 50 km. It is located in the westernmost end of OTZ, which is marked by SZF (F8 in Fig. 2), the boundary fault of the Shuicheng-Ziyun Aulacogen (SZA). SZA is an NW-trending Paleozoic aulacogen, which is featured by a notable linear basin with an approximate dimension of 400-km long and ca. 10-80-km wide (Wang et al., 2006). SZA plays important roles in the crustal evolution and the ore-forming process in Western Guizhou. Given the consistency of the features between the signature CB and the realistic SZA, we interpret the signature CB as the crystalline basement of SZA. Wang et al. (2006) investigated the sedimentary filling succession and suggested that the aulacogen was initiated at the early Devonian and was uplifted during the volcanism of ELIP with differential erosion during the late middle Permian. As a result of the Dongwu Movement in South China (He et al., 2010), the surface uplift reached up to 200-400 m, as estimated by the unconformity between the upper and middle Permian paleokarst formations (Wang et al., 2006).

5.2.3. Conrad discontinuity (CD)

The signature CD marks the continuous positive amplitudes at ca. 2.5-3.0 s (Fig. 4) or at the depth ca. 20-25 km (Fig. 5c). It appears in the whole IMZ and in the east part of INZ, bounded by LYF (F5 in Fig. 2) to the west and by SZF (F8 in Fig. 2) to the east flanks and is absent in the west part of INZ (Figs. 4, 5c). The depth range (20-25 km) that CD appears at corresponds to the base of the upper crust (Fig. 5d) that is revealed by the COMWIDE-ELIP experiment (Xu et al., 2015), and thus it is likely the Conrad discontinuity that is considered to be the interface between the upper and the lower continental crust. The features on the appearance and termination of the upper crustal reflectivity were also recognized by the previous controlled-source seismic survey mentioned above (Xiong, et al., 1986). Therefore, we interpret the signature CD as the Conrad discontinuity in the east part of INZ and throughout IMZ.

5.2.4. Underplating interface (UI)

The signature UI marks the continuous positive amplitudes at 4.5-5.0 s (Fig. 4) or at the depth of ca. 35 km (Fig. 5c). It appears in INZ with 150-180 km east-west extent and 15-20 km thickness above Moho. It is characterized by the distinct bulk crustal properties of high Bouguer gravity anomaly (Fig. 5a), high P-wave velocity (Fig. 5b, d), high Vp/Vs ratio and low heat flow (Fig. 5f), and the large crustal thickness that is clearly divergent from the Airy Moho (Fig. 5e). The local Bouguer gravity anomaly in INZ has a wavelength (λ) of ca. 200-250 km (Fig. 5a), which can place an indirect constraint on the depth (z) of density anomaly in a first-order approximation by

$$\lambda \sim 2\pi z \quad (2)$$

Therefore, the depth of this density anomaly is estimated to be 30-40 km, which is consistent with the depth of the signature UI that is observed here (Fig. 5c) and that of the high velocity layer (HVL, 7.0-7.2 km/s) that appears in the crustal P-wave velocity section (Fig. 5d). Deng et al. (2014) investigated the residual gravity anomaly in South China and its relationship to ELIP. They found that the inverted density anomaly of ELIP is +0.06 g/cm^3 in INZ and decreases to approximately +0.03 g/cm^3 in OTZ. Recently, a new gravity inversion has been conducted based on the observations of our COMGRA-ELIP experiment (Deng et al., 2015). The positive gravity anomaly in INZ (Fig. 5a) was well fitted with a dense layer of ca. 3.14 g/cm^3

above Moho that extends at a depth of approximately 41 km. The observed positive residual gravity and the corresponding high density (Deng et al., 2014; 2015), high velocity, high Vp/Vs, and low heat flow (Fig. 5) can be attributed to cooled mafic/ultramafic rocks generated by large-scale magmatic intrusion (Thybo and Artemieva, 2013; Furlong and Chapman, 2013). Hence, accounting for these distinct crustal properties (high Vp/Vs ratio, high density, high P-wave velocity, low heat flow, and large crustal thickness) as the discriminator for the underplated intrusive mafic materials in INZ, we interpret the signature UI as the interface of the magmatic underplating that is related to the Permian mafic LIP.

5.3. Crustal underplating and vertical growth

The mantle plume hypothesis provides a simple explanation for the essential features of classic LIPs, and its predictions have been confirmed by many observations (Campbell, 2005). The multidisciplinary data obtained in ELIP argue for the existence of a Permian mantle plume (Xu et al., 2007; Ali et al., 2010). Magmatic underplating is an integrated part of the continental flood basalt (CFB) volcanism (Furlong and Foutain, 1986). It has been suggested that most of the magma that reaches the crust could solidify as underplated material and remain hidden underneath some LIPs (Cox, 1980, 1993; Thybo and Artemieva, 2013). The interaction of the mantle plumes with the continental lithosphere could play an important role in the lithospheric growth, modification and destruction, both at the plate margins and in the intraplate regions (Sun, 1989; Albarede, 1998). The mantle melting and infiltration of the basaltic magmas are not restricted to the mantle part of the lithosphere, but often result in emplacement of magmatic bodies into the crust or at its base, i.e. crustal underplating (Cox, 1980, 1993; Furlong and Fountain, 1986; Fyfe, 1992; Thybo and Artemieva, 2013). This process could not only enhance the crustal growth from below by the addition of high density material to the deep crust (Rudnick, 1990), but also introduce the vertical growth within the upper parts of the crust by physical (e.g., thermal density buoyancy) and chemical (e.g., melting, crystallization, and differentiation) effects that are associated with the subsequent magmatism process until its eruption at the surface (Cox, 1980, 1993; Furlong and Fountain, 1986; Rudnick, 1990; Xu and He, 2007; Thybo and Artemieva, 2013). If the crustal underplating is related to the strong interaction that is triggered by the dynamic and thermal effects of the plume activity (Campbell, 2005), then the position where the plume head used to be located would have fossilized characteristics associated with the past magmatism process.

Besides the sedimentary features (He et al., 2003, 2010), other convincing evidences, such as the incompatible trace element contents of the picrites and basalt (Chung and Jahn, 1995), and the distributions of high-Ti and low-Ti lavas in ELIP (Xu et al., 2004) also suggested INZ was close to the plume axis at the time of volcanism. The distinct crustal properties and geometry (Fig. 5) that were obtained by our targeted geophysical investigations in INZ have been discussed above. The continuation of the signature CD at the base of the upper crust in INZ is terminated where the signature UI starts to appear (Fig. 5c). A similar observation made by Xiong et al. (1986) in an early controlled-source seismic survey showed that the upper crust in this region is transparent and free of upper crustal reflectivity. We interpret the lack of the signature CD and the appearance of the signature UI in INZ as the result of magmatic intraplating during the Emeishan volcanism (Xu and He, 2007).

In INZ, where the plume head is expected to be located, the extent of mantle melting (and consequently melt volume) is much larger than in IMZ and OTZ. A larger degree of melting not only generated thicker volcanic successions in INZ, but also produced unusual crustal properties in this region as illustrated in Fig 5. The addition of magmas at various levels of the crust and the subsequent interactions with the pre-existing crust might have considerably modified the crustal properties and demolished its original crustal geometry, such as signature CD that is observed in IMZ (Fig. 8). This argument is further supported by other independent studies. Chen et al. (2013) found that there is a coherent relationship between the deep crustal deformation by crustal anisotropy (Pms splittings) and the shallow deformation by GPS movement in INZ. Such a strong coupling between the shallow and deep parts of the crust most likely reflects the strong vertical interaction that is related to the plume activity.

The topographic uplift is the most dramatic surface expression for the vertical crustal growth. The addition of voluminous basic magma to the lithospheric column would cause a permanent surface uplift. Assuming a perfect Airy-type isostatic equilibrium, the amount of uplift u (Shoko and Gwavava, 1999), can be estimated by

$$u = (1.0 - \rho_x/\rho_a)x \quad (3)$$

where, x and ρ_x are the thickness and density of the added material, respectively, and ρ_a is the density of the asthenosphere (ca. 3.4 g/cm^3 generally). In our case, x is ca. 15-20 km (Fig. 5c) and ρ_x is ca. 3.14 g/cm^3 (Deng et al., 2015). Hence, the uplift u can be estimated as approximately 1000-1500 m. Furthermore, assuming a complete melt segregation and accumulation, Furlong and Fountain (1986) evaluated the potential for crustal underplating to increase the total thickness of the crust by the deep melt. The modeling results indicated that if more than 15 km thick mantle-derived materials are added to the crust at depths of 30 to 50 km, the melt-generation depth would be greater than 125 km, which is already below the 110-km depth of the lithosphere-asthenosphere boundary (LAB) beneath INZ, as imaged by S-wave RFs (Chen et al., 2015). According to our observation, a 15-20 km thick layer is the minimum estimate of the added materials through magmatic underplating in INZ (Fig. 5c), because the volumes of massive eruption and accumulation (magma dykes) within the upper parts of the crust are not included. Therefore, not only the surface uplift but also the melt-generation depth related to the crustal underplating would be much larger than the estimate made above.

He et al. (2003) carried out the biostratigraphic and sedimentologic investigations for the middle Permian Maokou Formation that immediately underlies the Emeishan flood basalts. A rapid, kilometer-scale crustal doming prior to the eruption of the Emeishan flood basalts is proposed with a time scale less than 3 Myr and a magnitude of uplift greater than 1000 m. Specifically, a layer of conglomerate of variable thickness is found underneath the main phase of the Emeishan basalts and above the earlier phase of basalts in the northeastern flank of the domal structure along the eastern boundary of the Xiaojiang fault (XJF, F6 in Fig. 2). It was suggested that the conglomerate layer was formed due to a differential uplift of the blocks in the northeastern flank of the domal structure, and thus, XJF would be a syn-doming normal fault that was deformed during the crustal doming period.

Because of the superposition of the subsequent tectonic movements (such as the ongoing Indo-Eurasian collision since Cenozoic), the present elevation of ELIP (upper panel of Fig. 5c) is in fact much higher than that estimated above either by the isostatic theory or by the sedimentary records. Meanwhile, the major faults in ELIP are characterized mainly by the kinematic and dynamic features that are related to the present-day tectonic settings. For example, the present movement of XJF is featured as left-lateral slipping (Yin, 2010). Based on the sedimentary records in ELIP (Wang et al., 2006; He et al., 2003; 2010), the kinematic features of the major faults (such as XJF, SZF) during the period of Permian volcanism could be unified into a dynamic framework that is related to the crustal vertical growth that results from the mafic-magma underplating, which was eventually related to the activity of the Permian ancient plume.

Fig. 8 is a cartoon that summarizes coherently the observations that regard the crustal structures and dynamic responses in ELIP. The hot buoyant mantle material ascended from the mantle toward the Earth's surface, penetrated into the crust and gave rise to large-scale crustal underplating that accumulated near the Moho. The Conrad discontinuity (CD in Fig. 8) that is observed in IMZ was diluted by the magmatic process in INZ. The Moho depth in INZ is in average greater than that of other zones (Figs. 4, and 7), with an approximately domal shape below the underplating layer (Figs. 5e, and 8). The deepest Moho, however, lies immediately east of the underplating zone. This feature may reflect some relics of the dynamic response of the impact that is related to the plume activity, and the recent crustal modification by the lateral compression induced by the India-Eurasia collision since Cenozoic. The consequence of all was a significant vertical growth within the crust. In addition to magmatic penetration into the crust, the mantle plume initiated kilometer-scale topographic uplift, thereby causing the domal deformation of the crust and activating some large regional faults.

6. Conclusions

Our comprehensive geophysical investigations revealed distinct features of the crustal nature and geometry in INZ of ELIP. Several distinct crustal properties, including high density, high P-wave velocity, high Vp/Vs ratio, low heat flow, a thick crust and the geometry of intra-crustal features, strongly support a mafic layer of 15-20 km thick and 150-180 km in lateral extent at the base of the crust in INZ,. This mafic layer is interpreted as a result of magmatic underplating related to the Permian mantle plume. The continuous seismic signature CD, which is interpreted as the

Conrad discontinuity, is present in the whole IMZ and in the eastern part of INZ, but is absent in the central and western parts of INZ. Instead, the seismic signature UI is observed in these areas and is interpreted as the interface of the underplating materials. Such a spatial configuration of the signatures UI and CD is attributable to the addition of plume-derived melts into the pre-existing crust and intensive interaction between them. Assuming a crustal isostacy, such large-scale magmatic underplating near the Moho would introduce a permanent kilometer-scale surface uplift, which is well recorded by the biostratigraphy of the pre-volcanic sediments. All of these findings, therefore, lend strong support to the mantle plume model that was proposed for the generation of ELIP.

Acknowledgments

We would like to express our sincere appreciation and deep-felt memory to our former group leader and good friend, Prof. Zhongjie Zhang, who suddenly passed away on September 6, 2013. Zhongjie was the principal scientist of the geophysical project on ELIP. Without his effort, inspiring ideas and continuous encouragement, this research would not have been initiated at the beginning and could not have been finally achieved. We thank the vehicle drivers, Lijun Wang and Changping Cai, and the other field personnel for their assistance during the field work. We also wish to thank Prof. Wei Tao for her contribution of the regional heat flow data, and Profs. Xiong Xiong, Bihong Fu, Rui Gao, Yanghua Wang, Fuqin Zhang, andCarlos López Casado for their helpful discussions. Constructive comments and suggestions from two anonymous reviewers significantly improved the quality of this paper. This study is financially supported by the National Basic Research Program of China (973 Program, grant 2011CB808904, 2011CB808906) and is also supported by the National Natural Science Foundation of China (grants 41374063 and 41074057). The Seismic Array Laboratory, IGGCAS, provided the instrumental equipment.

References

Albarede, F., 1998. The growth of continental crust. Tectonophysics 296, 1-14.

Ali, J.R., Fitton, J.G., Herzberg, C., 2010. Emeishan large igneous province (SW China) and the mantle-plume up-doming hypothesis. J. Geol. Soc. Lond. 167, 953-

959.

Ali, J.R., Thompson, G.M., Zhou, M.F., Song, X.Y., 2005. Emeishan large igneous province, SW China. Lithos 79, 475-489.

Bao, X.W., Sun, X.X, Xu, M.J., Eaton, D.W., Song, X.D., Wang, L.S., Ding, Z.F., Mi, N., Li, H., Yu, D.Y., Huang, Z.C., Wang, P., 2015. Two crustal low-velocity channels beneath SE Tibet revealed by joint inversion of Rayleigh wave dispersion and receiver functions. Earth Planet. Sci. Lett. 415, 16-24.

Bryan, S.E., Riley, T.R., Jerram, D.A., Stephens, C.J., and Leat, P.T., 2002. Silicic volcanism: An undervalued component of large igneous provinces and volcanic rifted margins, in Menzies, M.A., Klemperer, S.L., Ebinger, C.J., and Baker, J., eds., Volcanic Rifted Margins: Boulder, Colorado, Geol. Soc. America Special Paper 362, p. 99-120.

Campbell, I.H., 2005. Large igneous provinces and the mantle plume hypothesis. Elements 1(5), 265-269.

Chen, Y., Zhang, Z.J., Sun, C.Q., and Badal, J., 2013. Crustal anisotropy from Moho converted Ps wave splitting analysis and geodynamic implications beneath the eastern margin of Tibet and surrounding regions. Gondwana Res. 24(3-4), 946-957.

Chen, Y., Yuan, X.H., Tian, X.B., Liang, X.F., Si, S.K., Xu, Y.G., Teng, J.W., 2015. Lithospheric structure and origin of the Emeishan Large Igneous Province (SW China) revealed by the COMPASS-ELIP experiment. Geochem. Geophys. Geosyst. (in preparation).

Christensen, N.I., 1996. Poisson's ratio and crustal seismology. J. Geophys. Res. 101(B2), 3139-3156.

Chung, S.L., Jahn B.M., 1995. Plume-lithosphere interaction in generation of the Emeishan flood basalts at the Permian-Triassic boundary. Geology 23, 889-892.

Cox, K.G., 1980. A model for flood basalt volcanism. J. Petro. 21(4), 629-650.

Cox, K.G., 1993. Continental magmatic underplating. Philos. Trans. R. Soc. Lond. 342, 155-166.

Deng, Y.F., Chen, Y., Wang, P., Essa, K.S., Xu, T., Tian, X.B., Liang, X.F, Badal, J., Teng, J.W., 2015. Magmatic underplating beneath the Emeishan Large Igneous Province (South China) revealed by the COMGRA-ELIP experiment. Tectonophysics (under review).

Deng, Y.F., Zhang, Z.J., Mooney, W., Badal, J., Fan, W.M., Zhong, Q., 2014. Mantle origin of Emeishan large igneous province (south China) from the analysis of residual gravity anomalies. Lithos 204, 4-13.

Efron, B., Tibshirani R., 1986. Bootstrap methods for standard errors, confidence intervals, and other measures of statistical accuracy. Statistical Science 1(1), 54-77.

Furlong, K.P., Chapman, D.S., 2013. Heat flow, heat generation, and the thermal state of the lithosphere. Annu. Rev. Earth Planet. Sci. 41: 385-410.

Furlong, K.P., Fountain, D.M., 1986. Continental crustal underplating: thermal considerations and seismic-petrologic consequences. J. Geophys. Res. 91(B8), 8285-8294.

Fyfe, W.S., 1992. Magma underplating of continental crust. J. Volcanol. Geotherm. Res. 50, 33-40.

Hawkesworth, C., Cawood, P., Dhuime, B., 2013. Continental growth and the crustal record. Tectonophysics 609, 651-660.

He, B., Xu, Y.G., Chung, S.L., Xiao, L., Wang, Y.M., 2003. Sedimentary evidence for a rapid, kilometer-scale crustal doming prior to the eruption of the Emeishan flood basalts. Earth Planet. Sci. Lett. 213, 391-405.

He, B., Xu, Y.G., Guan, J.P., Zhong, Y.T., 2010. Paleokarst on the top of the Maokou Formation: further evidence for domal crustal uplift prior to the Emeishan flood volcanism. Lithos 119, 1-9.

He, C.S., Santosh, M., Wu, J.P., Chen, X.H., 2014. Plume or no plume: Emeishan Large Igneous Province in Southwest China revisited from receiver function analysis. Phys. Earth Planet. Int. 232, 72-78.

Hu, S.B., He, L.J., Wang, J.Y., 2000. Heat flow in the continental area of China: a new data set. Earth Planet. Sci. Lett. 179, 407-419.

Kennett, B.L.N., Engdahl, E.R., 1991. Traveltimes for global earthquake location and phase identification. Geophys. J. Int. 105, 429-465.

Lei, J.S., Zhao, D.P., Su, Y.J., 2009. Insight into the origin of the Tengchong intraplate volcano and seismotectonics in southwest China from local and teleseismic data. J. Geophys. Res. 114, B05302, doi:10.1029/2008JB005881.

Ligorria, J.P., Ammon, C.J., 1999. Iterative deconvolution and receiver-function estimation. Bull. Seismol. Soc. Am. 89, 1395-1400.

Mckenzie, D., 1984. A possible mechanism for epeirogenic uplift. Nature 307, 616-618.

Montelli, R., Nolet, G., Dahlen, F.A., Masters, G., Engdahl, E.R., Huang, S.H., 2004. Finite-frequency tomography reveals a variety of plumes in the mantle. Science 303, 338-343.

Royden, L.H., Burchfiel, B.C., King, R.W., Wang, E., Chen, Z.L., Shen, F., Liu, Y.P., 1997. Surface deformation and lower crustal flow in Eastern Tibet. Science 276, 788-790.

Rudnick, R., 1990. Growing from below. Nature 347, 711-712.

Shoko, D.S.M., Gwavava, O., 1999. Is magmatic underplating the cause of post-rift uplift and erosion within the Cabora Bassa Basin, Zambezi Rift, Zimbabwe? J. African Earth Sci. 28(2), 465-485.

Sun, S.S., 1989. Growth of lithospheric mantle. Nature 340, 509-510.

Sun, X.X., Bao, X.W., Xu, M.J., Eaton, D.W., Song, X.D., Wang, L.S., Ding, Z.F., Mi, N., Yu, D.Y., Li, H., 2014. Crustal structure beneath SE Tibet from joint analysis of receiver functions and Rayleigh wave dispersion. Geophys. Res. Lett. 41, 1479-1484.

Tao W, Shen Z.K., 2008. Heat flow distribution in Chinese continent and its adjacent areas. Progress in Natural Science 18, 843-849.

Thybo, H., Artemieva, I.M., 2013. Moho and magmatic Underplating in continental lithosphere. Tectonophysics 609, 605-619.

Wang, S.Y., Zhang, H., Wang, T.H., Wang, C.H., Peng, C.L., Hu, R.F., Chen, M.H., Shi, L., 2006. Filling and evolution of the Late Paleozoic shuicheng-Ziyun aulacogen in western Guizhou, China. Geological Bulletin of China 25(3), 402-407 (in Chinese with abstract in English).

Wignall, P.B., Sun, Y.D., Bond, D.P.G., Izon, G., Newton, R.J., Vedrine, S., Widdowson, M,, Ali, J.R., Lai, X.L., Jiang, H.S., Cope, H., Bottrell, S.H., 2009. Volcanism, mass extinction, and carbon isotope fluctuations in the middle Permian of China. Science 324, 1179-1182.

Xiong, S.B., Teng, J.W., Yin, Z.X., Lai, M.H., Huang, Y.P., 1986. Explosion seismological study of the structure of the crust and upper mantle at southern part of the Panxi tectonic belt (in Chinese with abstract in English). Chinese J. Geophys. 29(3), 235-244.

Xu, T., Zhang, Z.J., Liu, B.F., Chen, Y., Zhang, M.H., Tian, X.B., Xu, Y.G., Teng, J.W., 2015. Crustal velocity structure in the Emeishan large igneous province and evidence of the Permian mantle plume activity. Sci. China-Earth Sci. 58(7), 1133-1147.

Xu Y.G., He, B., Chung, S.L., Menzies, M.A., Frey, F.A., 2004. Geologic, geochemical, and geophysical consequences of plume involvement in the Emeishan flood-basalt province. Geology 32(10), 917-920.

Xu, Y.G., He, B., 2007. Thick, high-velocity crust in the Emeishan large igneous province, southwestern China: Evidence for crustal growth by magmatic underplating or intraplating. GSA Special Papers 430, 841-858.

Xu, Y.G., He, B., Huang, X.L., Luo, Z.Y., Chung, S.L., Xiao, L., Zhu, D., Shao, H., Fan, W.M., Xu, J.F., Wang, Y.J., 2007. Identification of mantle plumes in the Emeishan Large Igneous Province. Episodes 30(1), 32-42.

Xu, Y.G., Wang, C.Y., Shen, S.Z., 2014. Permian large igneous provinces: Characteristics, mineralization and paleo-environment effects. Lithos 204, 1-3.

Xu, Z.J., Song, X.D., 2010. Joint inversion for crustal and Pn velocities and Moho depth in Eastern Margin of the Tibetan Plateau. Tectonophysics 491, 185-193.

Yin A., 2010. Cenozoic tectonic evolution of Asia: A preliminary synthesis. Tectonophysics 488, 293-325.

Yuan, X., Ni, J., Kind, R., Mechie, J., Sandvol, E., 1997. Lithospheric and upper mantle structure of southern Tibet from a seismological passive source experiment. J. Geophys. Res. 102, 27491-27500.

Zandt, G., Ammon, C.J., 1995. Continental crust composition constrained by measurements of crustal Poisson's ratio. Nature 374, 152-154.

Zhong, Y.T., He, B., Mundil, R., Xu, Y.G., 2014. CA-TIMS zircon U-Pb dating of felsic ignimbrite from the Binchuan section: Implications for the termination age of Emeishan large igneous province. Lithos 204, 14-19.

Zhou, M.F., Arndt, N.T., Malpas, J., Wang, C.Y., Kennedy, A.K, 2008. Two magma series and associated ore deposit type in the Permian Emeishan large igneous province, SW China. Lithos 103, 352-368.

Zhu, L.P., Kanamori, H., 2000. Moho depth variation in southern California from teleseismic receiver functions. J. Geophys. Res. 105, 2969-2980.

Table caption

Table 1. The average crustal thickness (H) and the bulk Vp/Vs ratio (κ) beneath each station of the COMPASS-ELIP seismic array.

Figure captions

Fig. 1. The emplacement site of Emeishan Large Igneous Province (ELIP) shown in a paleogeographic map of late Permian (a) (modified from Ali et al., 2005) and its present location (b) with other LIPs exposed on the Earth (modified from Bryan et al., 2002). Note the very large dimensions that the ELIP has traveled in space and time since its formation and, hence, the mismatch between the locations of the Permian plume source and the present-day ELIP and the exhaustion of thermal effect in ELIP.

Fig. 2. Shaded topographic map that shows the regional geologic features in ELIP and the location of the COMPASS-ELIP seismic array. The red triangles with black frames indicate the stations in the West-Line, which were operated from November 2010 to November 2011. The red triangles without outlines indicate the stations in the East-Line, which were operated from December 2011 to April 2013. The gray thick line indicates the location of the COMWIDE-ELIP experiment (Xu et al., 2015). The green areas show the distribution of ELIP basalts. The upper-right inset

is a map of East Asia, in which a red bar indicates the approximate location of the array. Abbreviations for faults: F1, Nujiang Fault; F2, Langcang Fault; F3, Ailaosan-Red River Fault (ARF); F4, Lijiang-Xiaojinghe Fault (LXF); F5, Lvzhijiang-Yuanmou Fault (LYF); F6, Xiaojiang Fault (XJF); F7, Shizong-Mile Fault; F8, Shuicheng-Ziyun Fault (SZF); F9, Zunyi-Guiyang Fault; and F10, Zhenyuan-Guiyang Fault. Abbreviations for zones: TRZ, Three-river Zone; INZ, Inner Zone; IMZ, Intermediate Zone; OTZ, Outer Zone. Acronyms in the upper-right inset: NCC, North China Craton; YC, Yangtze Craton; and ICB, Indo-China Block.

Fig. 3. Map of events with magnitudes of Ms > 5.0 and epicentral distances between 30° and 90° used in this study. The red circles indicate 579 events recorded by the West-Line of the array (Fig. 2), while the green circles indicate 398 events recorded by the East-Line of the array. The red triangle with black frame indicates the approximate location of the COMPASS-ELIP array.

Fig. 4. Stacked receiver function profile in time-domain obtained by the stacking of move-out corrected traces in 50-km-width moving longitude bins with an overlapping step of 10 km, and based on the locations of the piercing point at 50 km depth. The inclined numbers at the bottom denote the numbers of stacked RFs for each bin. The geological features are marked on the top at their corresponding locations in Fig. 2. The labeled gray dashed lines indicate the signature that is

recognized in Fig. 5. Abbreviations for faults: ARF, Ailaoshan-Red River Fault; LXF, Lijiang-Xiaojinghe Fault; LYF, Lvzhijiang-Yuanmou Fault; XJF, Xiaojiang Fault; and SZF, Shuicheng-Ziyun Fault.

Fig. 5. Multidisciplinary geophysical observations along the profile. (a) Gravity anomaly derived from the COMGRA-ELIP experiment (Deng et al., 2015). The blue circles denote the Bouguer gravity. The red circles denote the residual Bouguer gravity, i.e., the remains of Bouguer gravity after subtracting the regional correction that was calculated by a one-order polynomial fit. (b) Averaged P-wave velocity derived from the crustal velocity section (d). (c) Migrated image of the crustal structure based on RFs. The stations of the COMPASS-ELIP experiment and topography along the profile are shown in the upper panel. The green line indicates the average topography along the profile computed by a running average within a 60-km radius. The signatures recognized here are the following: crystalline basement (CB), Conrad discontinuity (CD), underplating interface (UI) and Moho. (d) Crustal P-wave velocity along the profile derived from the COMWIDE-ELIP experiment (Xu et al., 2015). (e) Crustal thickness derived from the H-κ stacking analysis of RFs (blue circles, also marked by the black circles in (c)), and the Moho depth estimated from the Airy isostatic equilibrium (Airy Moho, green line) based on the average topography along the profile. (f) Vp/Vs ratios (blue circles) derived from the H-κ analysis of RFs, and heat flow (red line) along the profile extracted

from the dataset that produced the heat flow map of Chinese continent and its adjacent areas (Hu et al., 2000; Tao and Shen, 2008). The vertical bars in (e) and (f) denote the standard errors of the arithmetic averages computed by the three-point sliding average within each zone along the profile. Note that, the Inner Zone is characterized by high density, high P-wave velocity, high Vp/Vs ratios, low heat flow, large crustal thickness that deviates from the Airy Moho, and no significant low-velocity zone within the crust. The abbreviations for the faults and zones are the same as in Figs. 2 and 4.

Fig. 6. The migrated RF profiles in depth-domain obtained by Common Conversion Point (CCP) stacking (Yuan et al., 1997) using the IASP91 model (a) and a 2D modified model (b). The modified model contains lateral variations in the bulk crustal Vp-velocity (Fig. 5b) derived from the COMWIDE-ELIP experiment (Xu et al., 2015) (Fig. 5d) and the bulk crustal Vp/Vs ratios (Fig. 5e) from H-κ stacking. The amplitude scale is the same for both profiles. The conversions are more sharply imaged and properly located with the modified model. The surface elevation, geological features and stations along the profile are marked in the top panel. The abbreviations for the faults and zones are the same as in Figs. 2 and 4.

Fig. 7. Crustal thickness (H) versus Vp/Vs ratios along the COMPASS-ELIP profile.

The values that are associated with the four zones were enclosed by individual best-fitting ellipses with the minimum area. The Crosses in different colors show the measurements at different zones. The diamonds at the center of each ellipse correspond to the average H and Vp/Vs ratio of the zone. As a reference, the gray dashed line indicates the Vp/Vs ratio of 1.75.

Fig. 8. Interpretative cartoon that summarizes the observations of the crustal structures and the dynamic responses in ELIP. The crustal skeleton is delineated by the seismic signatures that were extracted from the migrated image (Fig. 5c). The inferred surface responses of the crustal vertical growth in the Inner Zone of ELIP at the time of the Permian magmatism are sketched without a strict scale. The green dashed line above the inferred surface indicates the flood basalts produced by the Permian volcanism. SZA: Shuicheng-Ziyun Aulacogen; SCLM: Subcontinental Lithospheric Mantle. The other abbreviations are the same as in Figs. 2 and 4.

Graphical Abstract (for review)

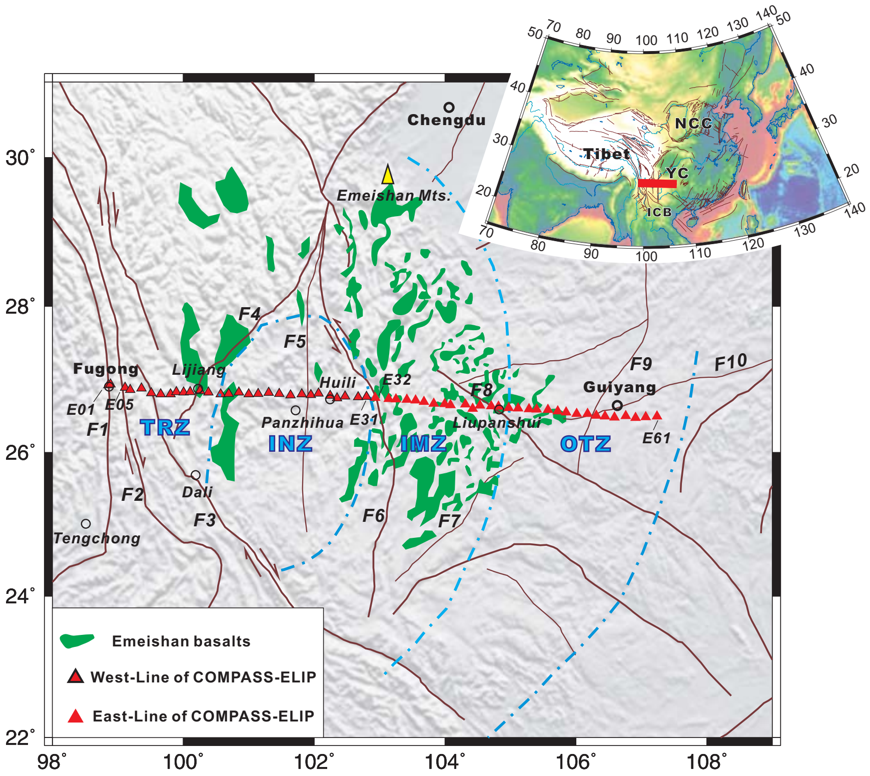

(a) Topographic map showing the regional geologic features in the Emeishan Large Igneous Province(ELIP) and the location of the seismic array.

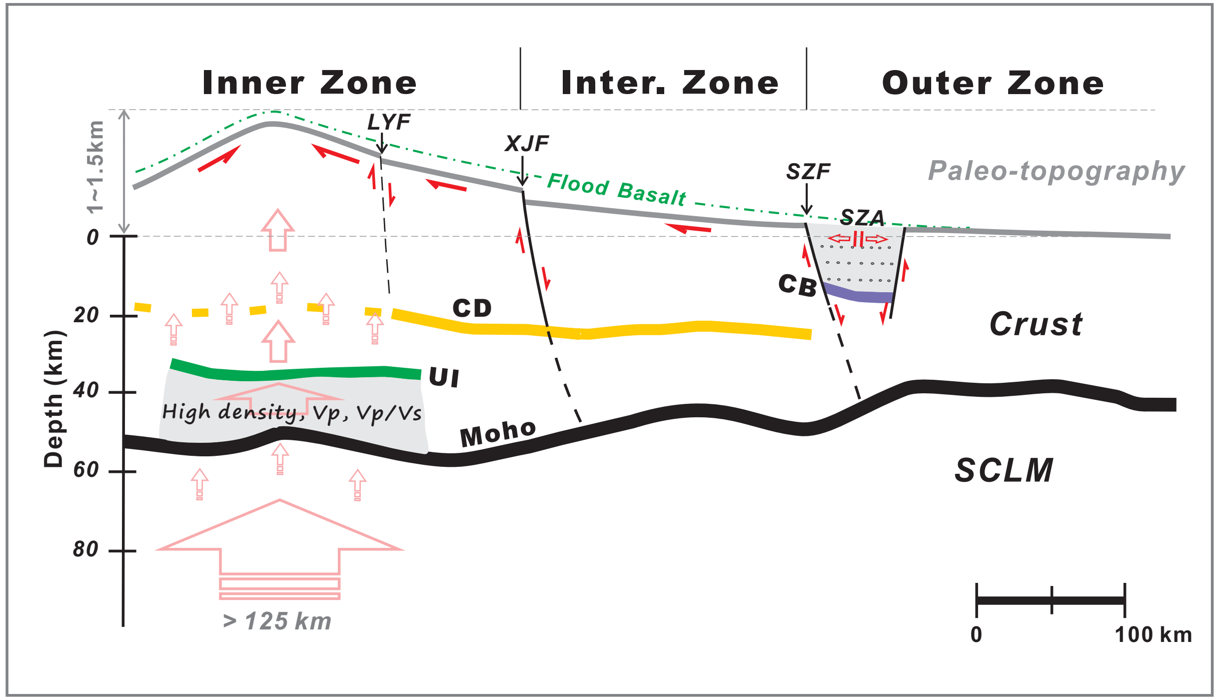

(b) Interpretative cartoon summarizing the observations of the crustal structures and the dynamic responses in ELIP.

Figure-01

Click here to download Figure: Fig01_R2.pdf

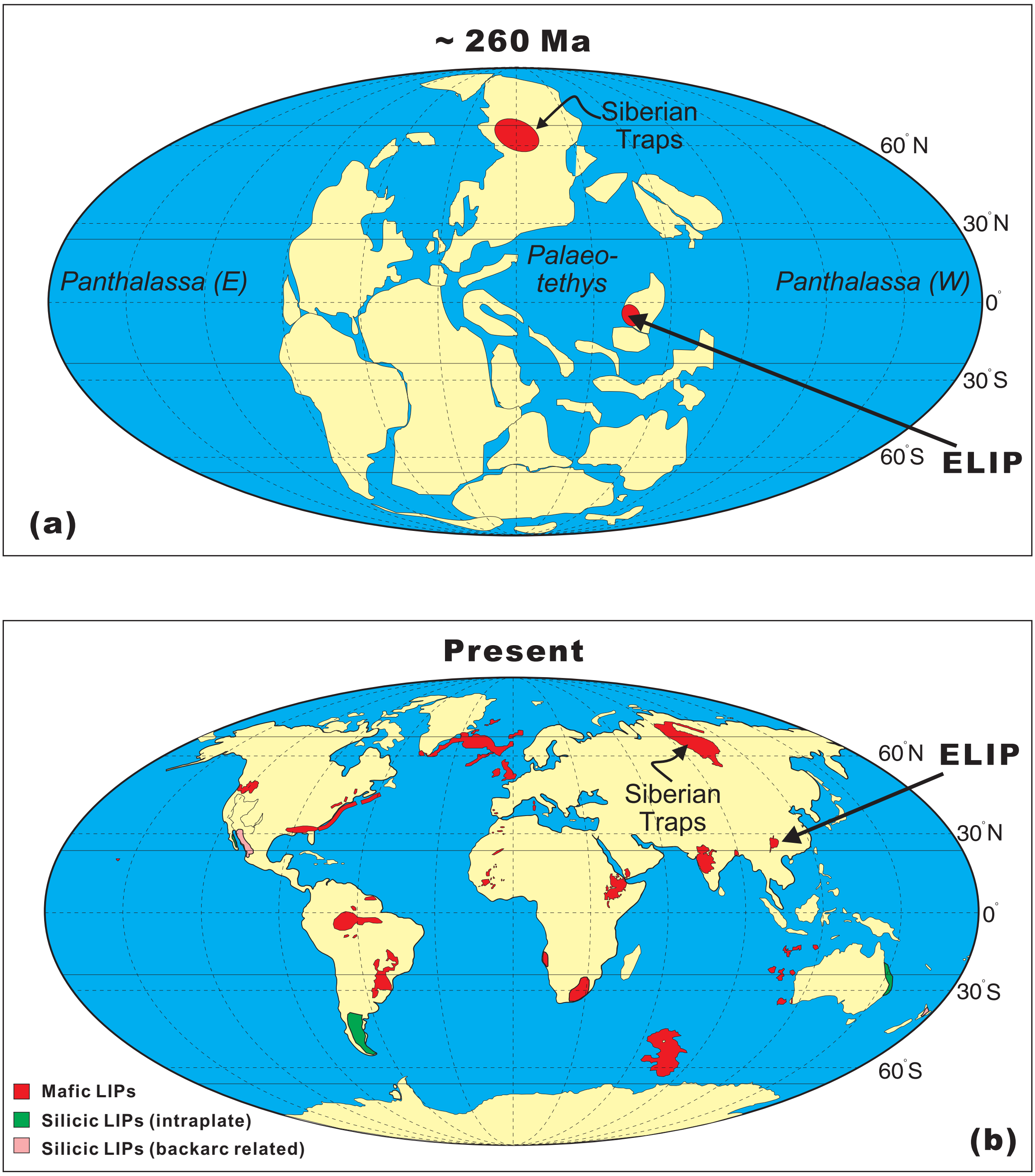

Figure-02
Click here to download Figure: Fig02_R2.pdf

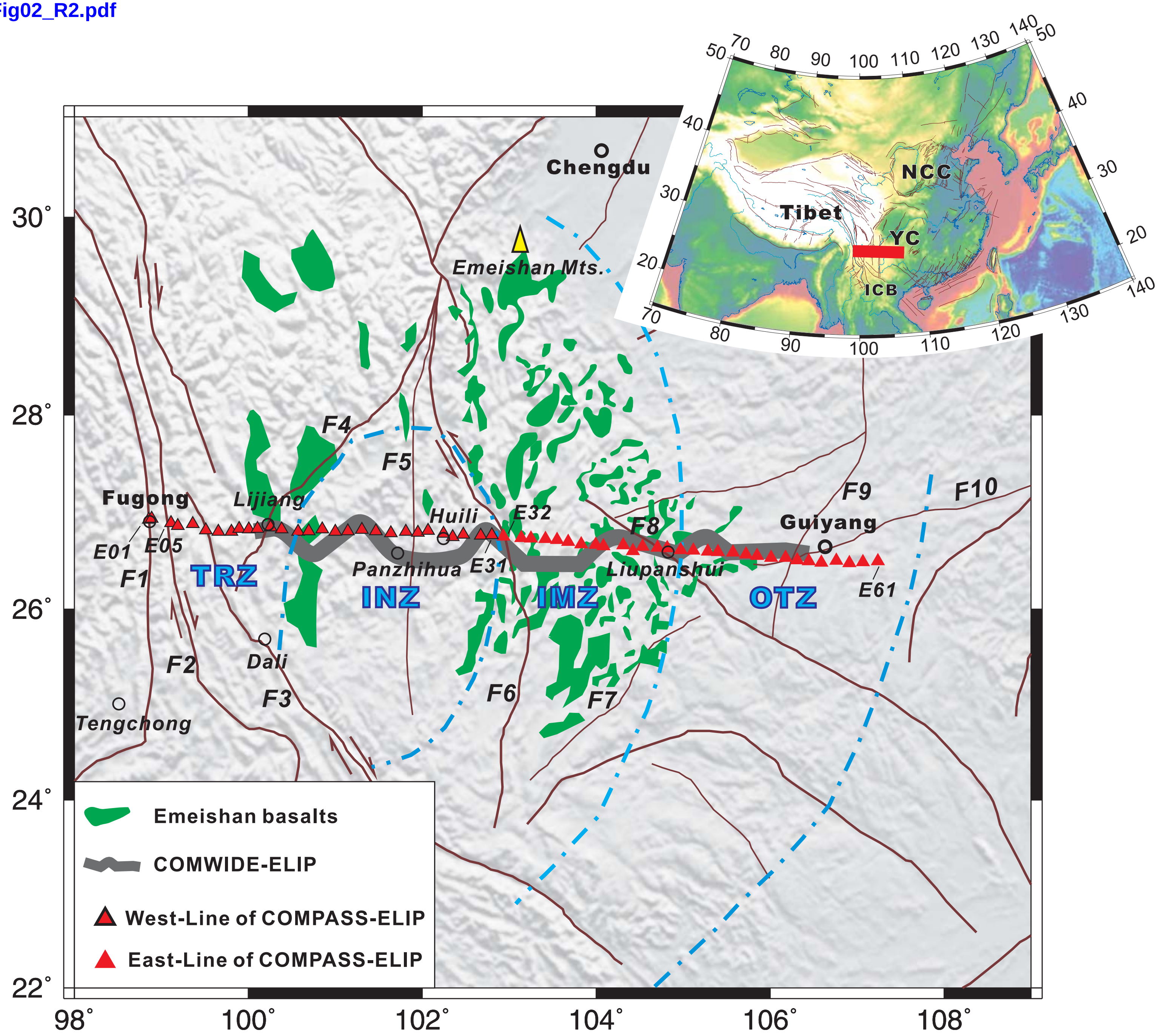

Figure-03

Click here to download Figure: Fig03_R2.pdf

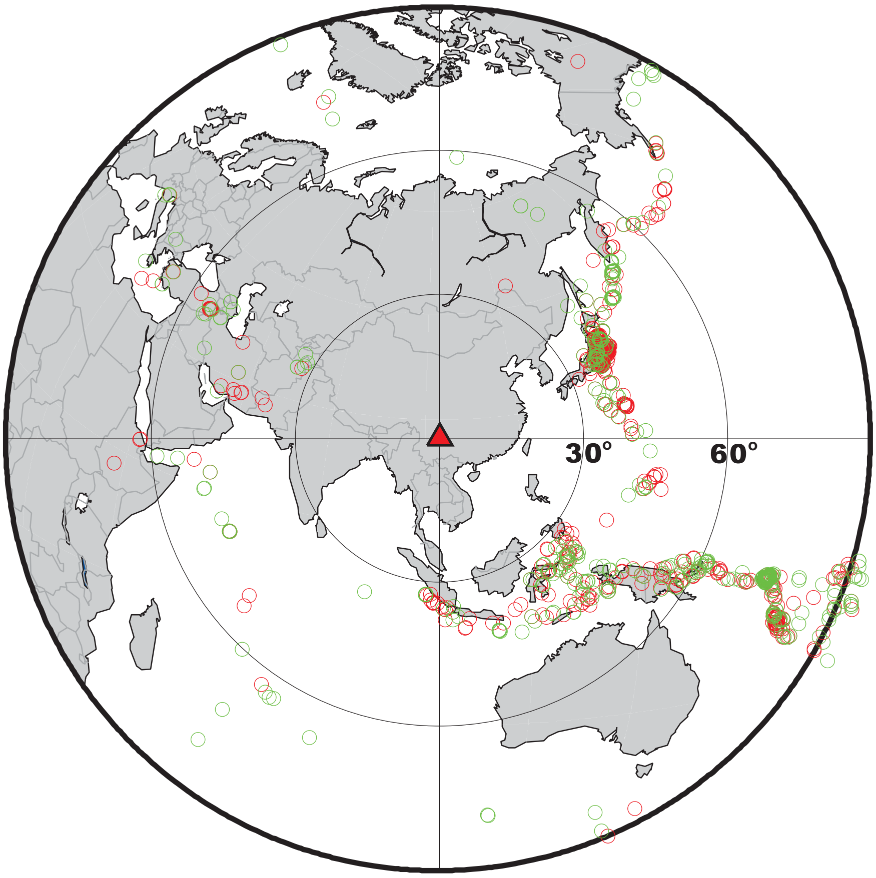

Figure-04

Click here to download Figure: Fig04_R2.pdf

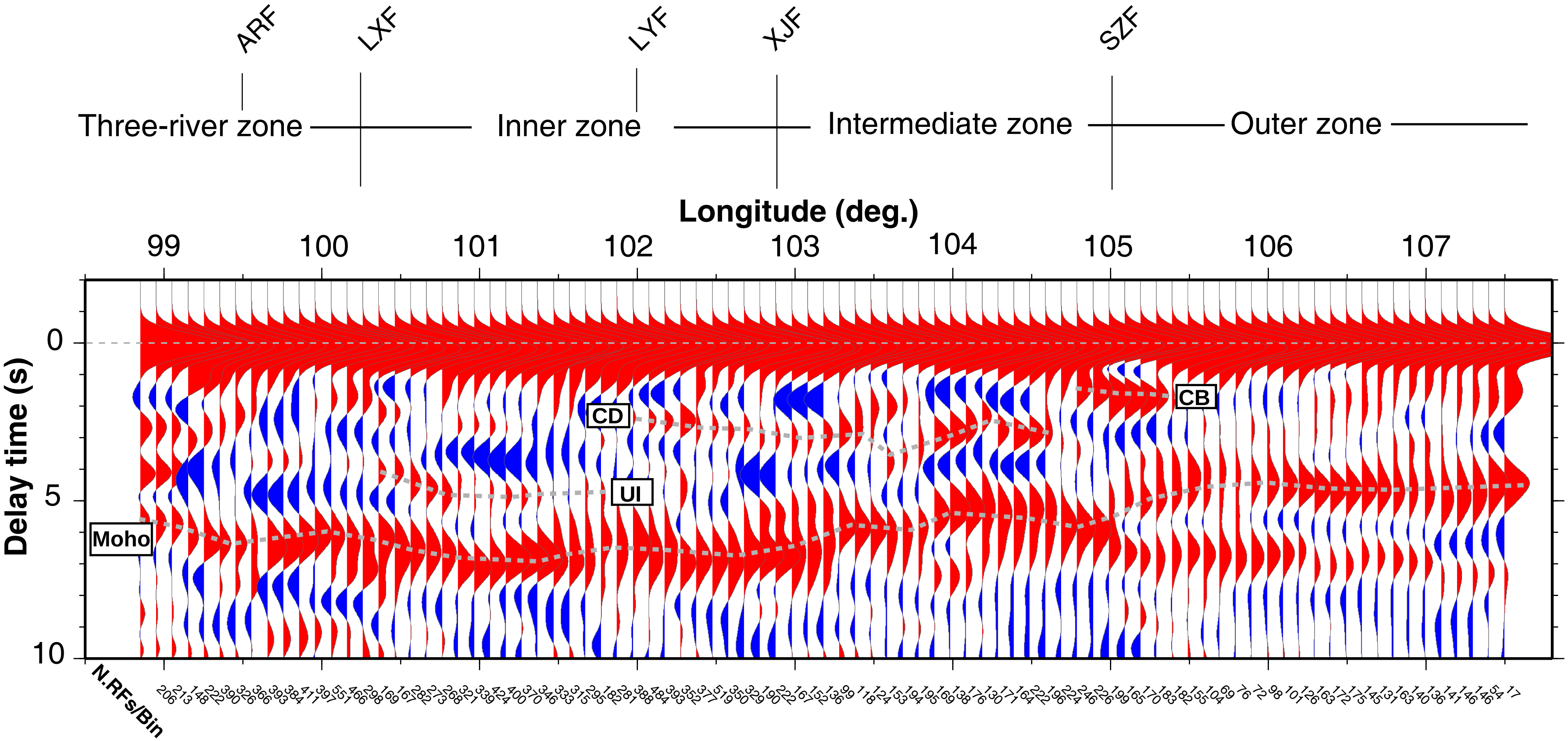

Figure-05

Click here to download Figure: Fig05_R2.pdf

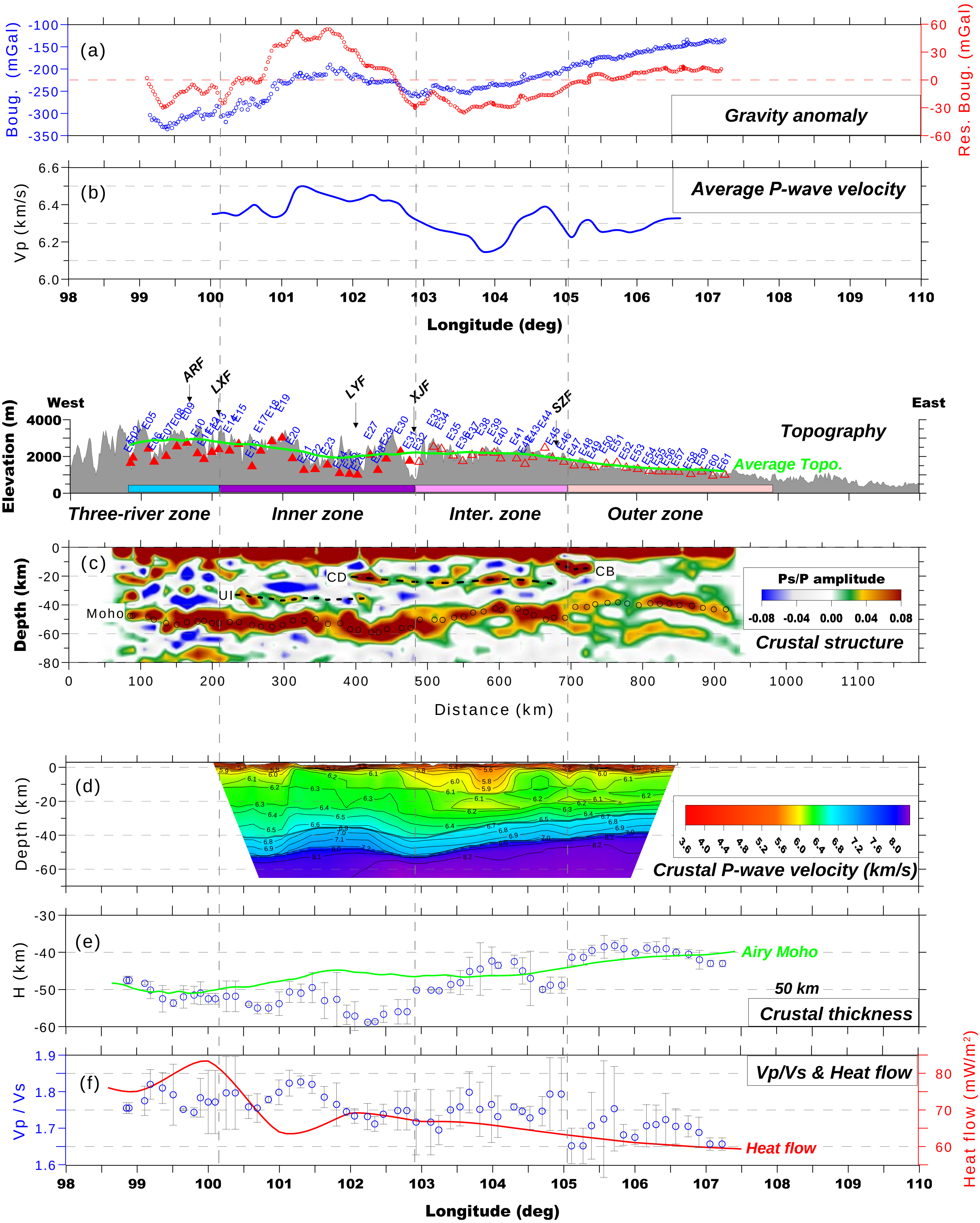

Figure-06

Click here to download Figure: Fig06_R2.pdf

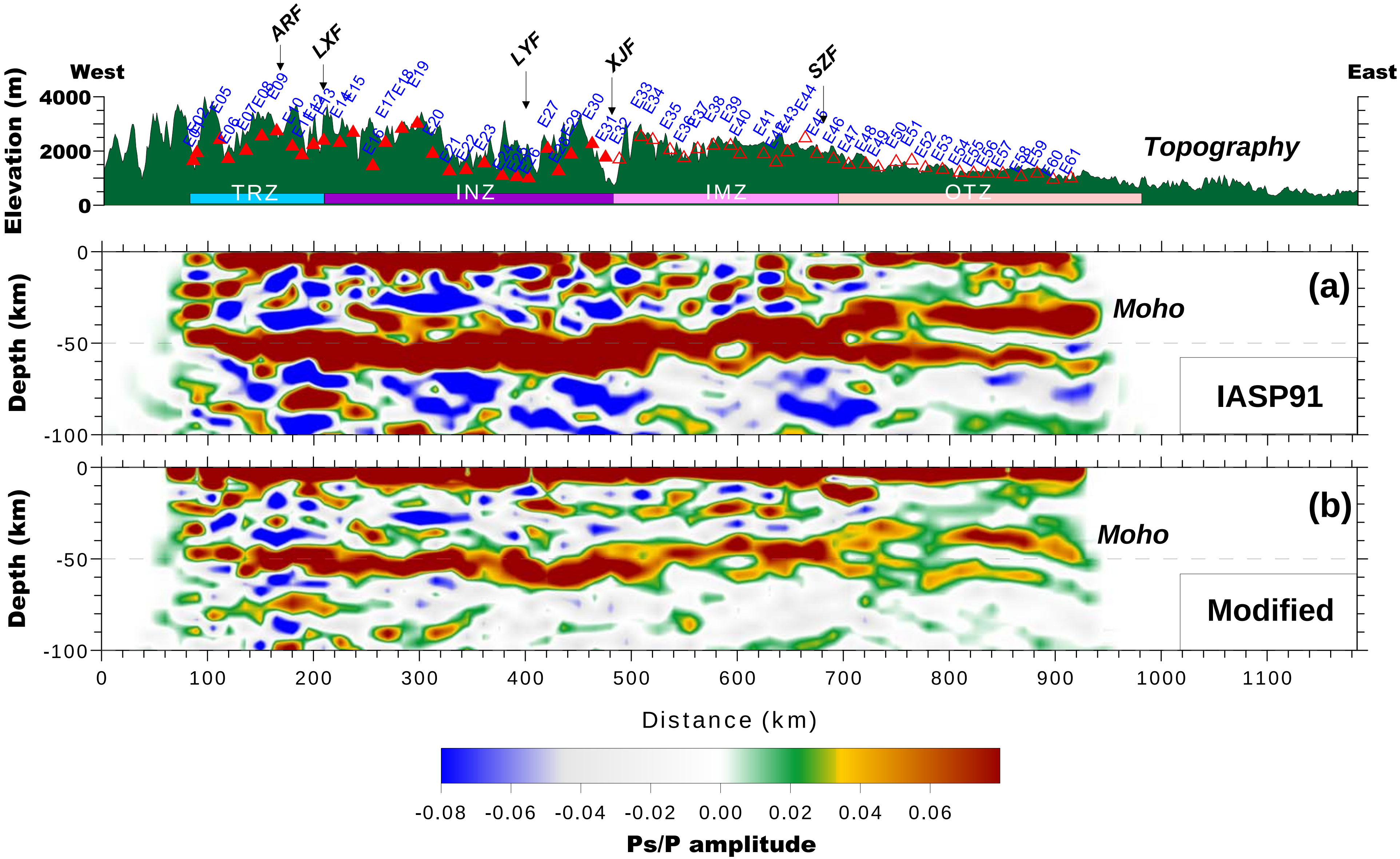

Figure-07

Click here to download Figure: Fig07_R2.pdf

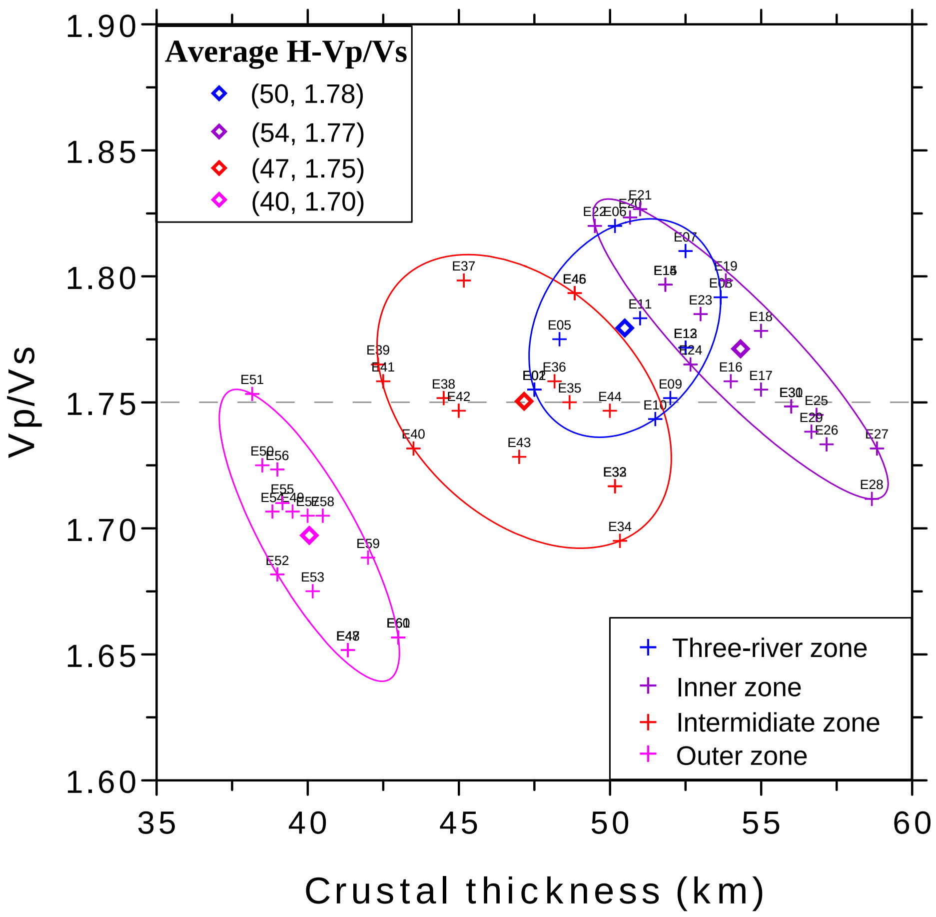

Figure-08

Click here to download Figure: Fig08_R2.pdf

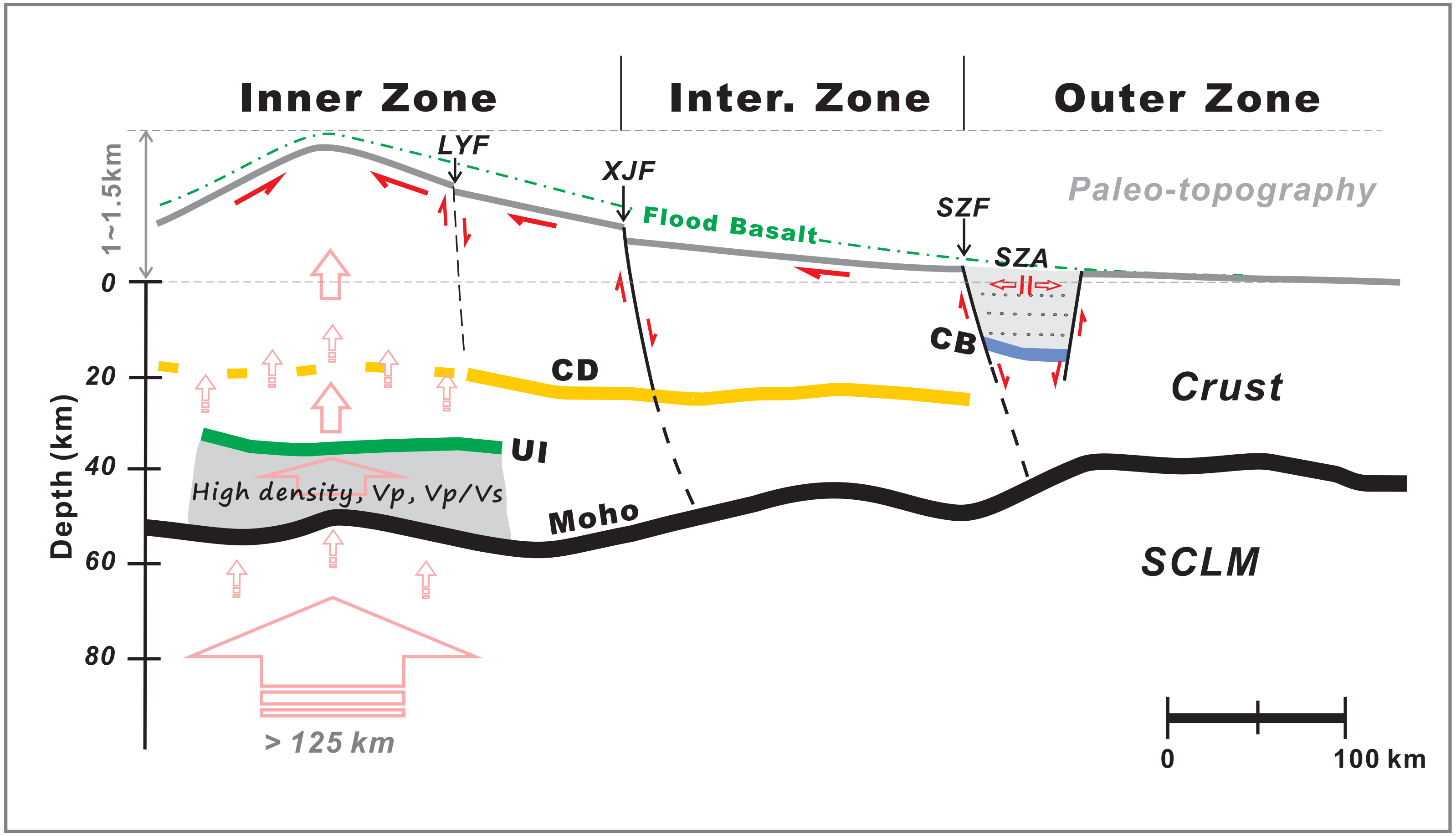

Table-01

Click here to download Table: table_01_R2.docx

Zone	Station	Longitude (°E)	Latitude (°N)	Elevation (m)	H-κ stacking [a] H (km)	H-κ stacking [a] Vp/Vs	Sliding average [b] H (km)	Sliding average [b] Vp/Vs	No. of RFs
Three-river	E01	98.855	26.927	1708	46.5±0.3	1.750±0.017	47.5±1.1	1.755±0.015	178
	E02	98.890	26.940	2002	48.0±3.5	1.735±0.044	47.5±1.1	1.755±0.015	26
	E05	99.110	26.892	2493	48.0±0.7	1.780±0.020	48.3±0.4	1.775±0.040	101
	E06	99.190	26.865	1782	49.0±0.3	1.810±0.010	50.2±2.3	1.820±0.041	115
	E07	99.361	26.884	2090	53.5±2.0	1.870±0.010	52.5±3.6	1.810±0.042	205
	E08	99.512	26.818	2618	55.0±0.3	1.750±0.010	53.7±1.0	1.792±0.084	166
	E09	99.654	26.803	2811	52.5±0.2	1.755±0.005	52.0±3.0	1.752±0.003	225
	E10	99.804	26.802	2240	48.5±0.1	1.750±0.004	51.5±2.3	1.743±0.013	162
	E11	99.895	26.835	1926	53.5±0.2	1.725±0.004	51.0±3.1	1.783±0.053	193
	E12	100.005	26.830	2307	51.0±0.2	1.875±0.007	52.5±1.5	1.772±0.087	206
	E13	100.103	26.834	2458	53.0±1.5	1.715±0.023	52.5±1.5	1.772±0.087	87
Inner	E14	100.258	26.848	2382	48.0±3.9	1.895±0.037	51.8±4.1	1.800±0.099	43
	E15	100.386	26.829	2748	54.0±0.5	1.775±0.009	51.8±4.1	1.800±0.099	139
	E16	100.573	26.805	1525	53.5±0.2	1.720±0.005	54.0±0.4	1.758±0.032	175
	E17	100.695	26.808	2378	54.5±0.2	1.780±0.005	55.0±1.5	1.755±0.039	85
	E18	100.852	26.827	2898	57.0±2.4	1.765±0.037	55.0±1.5	1.778±0.010	204
	E19	101.000	26.803	3090	53.5±0.2	1.790±0.009	53.8±3.2	1.798±0.033	223
	E20	101.146	26.806	1971	51.0±0.2	1.840±0.004	50.7±2.8	1.823±0.035	189
	E21	101.307	26.824	1333	47.5±3.2	1.840±0.059	51.0±2.5	1.827±0.016	167
	E22	101.466	26.809	1374	54.5±0.2	1.800±0.005	49.5±4.1	1.820±0.024	173
	E23	101.639	26.790	1618	46.5±1.9	1.820±0.017	53.0±4.8	1.785±0.029	125
	E24	101.812	26.804	1160	58.0±0.5	1.735±0.010	52.7±7.2	1.765±0.059	156
	E25	101.951	26.795	1118	53.5±0.2	1.740±0.006	56.8±2.6	1.745±0.011	247
	E26	102.065	26.813	1074	59.0±0.3	1.760±0.005	57.2±3.9	1.733±0.020	149
	E27	102.247	26.784	2158	59.0±3.2	1.700±0.044	58.8±0.2	1.732±0.036	188
	E28	102.350	26.747	1333	58.5±1.9	1.735±0.019	58.7±0.4	1.712±0.020	181
	E29	102.470	26.772	1950	58.5±0.6	1.700±0.017	56.7±2.2	1.738±0.027	176
	E30	102.673	26.761	2335	53.0±0.3	1.780±0.005	56.0±3.3	1.748±0.053	160
	E31	102.801	26.768	1834	56.5±0.6	1.765±0.015	56.0±3.3	1.748±0.053	59
Intermediate	E32	102.932	26.751	1771	50.0±3.4	1.795±0.049	50.2±0.2	1.717±0.090	117
	E33	103.138	26.739	2598	50.0±1.3	1.655±0.050	50.2±0.2	1.717±0.090	36
	E34	103.251	26.734	2481	50.5±1.2	1.700±0.016	50.3±0.4	1.695±0.040	65
	E35	103.415	26.728	2118	50.5±2.1	1.730±0.022	48.7±2.2	1.750±0.052	59
	E36	103.5493	26.716	1816	45.0±4.2	1.820±0.064	48.2±3.2	1.758±0.052	86
	E37	103.680	26.700	2146	49.0±1.3	1.725±0.022	45.2±3.8	1.798±0.056	85
	E38	103.829	26.676	2282	41.5±4.0	1.850±0.070	44.5±7.1	1.752±0.074	89
	E39	103.993	26.667	2266	43.0±1.7	1.680±0.033	42.3±3.8	1.765±0.104	45
	E40	104.082	26.655	1957	42.5±1.4	1.765±0.027	43.5±0.9	1.732±0.057	84
	E41	104.309	26.662	1962	45.0±1.5	1.750±0.042	42.5±1.8	1.758±0.009	108
	E42	104.425	26.604	1662	40.0±0.5	1.760±0.014	45.0±3.5	1.747±0.010	100
	E43	104.535	26.647	2035	50.0±0.9	1.730±0.014	47.0±7.3	1.728±0.032	63
	E44	104.706	26.637	2547	51.0±0.3	1.695±0.007	50.0±0.7	1.747±0.040	139
	E45	104.816	26.632	1966	49.0±1.1	1.815±0.054	48.8±2.2	1.793±0.100	95
	E46	104.975	26.616	1782	46.5±0.4	1.870±0.008	48.8±2.2	1.793±0.100	82
Outer	E47	105.119	26.606	1580	42.0±1.0	1.700±0.022	41.3±2.1	1.652±0.048	82
	E48	105.282	26.597	1592	39.5±1.6	1.655±0.022	41.3±2.1	1.652±0.048	103
	E49	105.401	26.595	1483	41.5±1.9	1.600±0.076	39.5±1.4	1.707±0.091	75
	E50	105.573	26.586	1672	37.5±3.3	1.865±0.020	38.5±3.1	1.725±0.159	38
	E51	105.721	26.571	1723	36.5±3.0	1.710±0.055	38.2±1.4	1.753±0.116	31
	E52	105.851	26.554	1455	40.5±1.4	1.685±0.081	39.0±2.7	1.682±0.028	39
	E53	106.012	26.531	1381	40.0±0.7	1.650±0.015	40.2±0.4	1.675±0.020	62
	E54	106.175	26.533	1283	40.0±0.4	1.690±0.008	38.8±1.4	1.707±0.058	51
	E55	106.309	26.511	1250	36.5±1.6	1.780±0.032	39.2±2.1	1.710±0.053	116
	E56	106.445	26.500	1242	41.0±0.6	1.660±0.013	39.0±2.9	1.723±0.072	61
	E57	106.586	26.484	1233	39.5±0.3	1.730±0.014	40.0±1.1	1.705±0.048	69
	E58	106.760	26.504	1114	39.5±0.4	1.725±0.024	40.5±1.2	1.705±0.029	98
	E59	106.914	26.480	1247	42.5±0.9	1.660±0.028	42.0±2.5	1.688±0.042	35
	E60	107.068	26.488	1020	44.0±0.3	1.680±0.012	43.0±0.9	1.657±0.017	116
	E61	107.239	26.500	1071	42.5±0.7	1.630±0.014	43.0±0.9	1.657±0.017	61

[a] Uncertainties are the standard errors estimated by bootstrap trials for each station; [b] Uncertainties are the standard errors estimated by sliding average for every three-station within each zone.